Dynamic Performance Enhancement of Power Converters in PV-battery Microgrids Based on Energy Control with Data-driven Compensation

Zhijun Zeng, Kaishun Xiahou, *Membership, IEEE*, Yang Liu, *Membership, IEEE*, Lei Wang, *Membership, IEEE*, Chuanyue Li, *Membership, IEEE*, Jun Liang, *Fellow, IEEE*, and Q. H. Wu, *Life Fellow, IEEE*

***Abstract*—Conventional control strategies for single-phase PV-battery microgrids often suffer from sluggish dynamic response due to reliance on synchronous coordinate frame transformations, and they struggle to maintain high power quality under transient grid conditions. To address these challenges, this paper proposes an energy-based control (EC) strategy that operates directly in the natural coordinate frame, thereby eliminating coordinate transformation delays and significantly accelerating dynamic response. Furthermore, to mitigate phase shift and harmonic distortion in the inverter output current, the EC framework integrates a phase compensation scheme and a data-driven passive harmonic compensation method. Comprehensive simulations and experimental results across multiple operational scenarios demonstrate that the proposed approach simultaneously enhances both transient performance and steady-state power quality, validating its effectiveness and practical viability for single-phase microgrid applications.**

***Index Terms*—PV-battery microgrids, bidirectional DC/DC converters, grid-connected inverters, dynamic response, energy control, data-driven compensation.**

I. Introduction

MICROGRIDS are regional energy systems that can operate independently or be connected to the power grid [1], [2]. With the proliferation of renewable energy technologies, microgrids are playing an increasingly important role in distribution systems. Due to the ease of integrating photovoltaic (PV) systems with other distributed energy resources and electric vehicles, PV systems have achieved the largest installed capacity in distribution systems. Since PV systems are greatly affected by weather, they are usually equipped with a battery energy storage system (BESS) to maintain uninterrupted power supply during the day, reduce power fluctuations and improve power quality [3]. Typically, such a PV-battery system forms a basic microgrid.

The energy generated by renewable sources is delivered to the grid or the load through converters [4]. Nonlinear components in transmission circuits adversely affect power quality, necessitating advanced control methods [5]. For BESS DC/DC converters, conventional PI control is predominantly used [6], [7]. However, its parameter limitations frequently fail to address rapidly fluctuating processes. Greater attention has focused on DC/AC inverters due to grid interconnection complexities. Grid-connected inverter (GCI) control methods are principally categorized as linear or nonlinear control methods.

For linear control methods, most work focuses on improving traditional PI control. Within this domain, the phase-locked loop (PLL) is a critical component for grid synchronization. Numerous PLL strategies, such as those based on second-order generalized integrators [8]–[11], have been developed. In small-signal stability analysis, the PLL's inherently nonlinear dynamics are typically linearized around an operating point for integration into a linear state-space model, allowing assessment of its impact on system modes. However, this linearized analysis reveals inherent limitations. When the grid frequency deviates from its nominal value, PLL-based synchronization degrades, leading to inaccurate phase tracking. Furthermore, the PLL's stability and response are highly sensitive to its internal PI parameters. Improper tuning can destabilize the PLL during fluctuations, cause adverse interactions with other system components, and degrade the damping of synchronous generator electromechanical modes, posing a risk to overall grid stability. For primary inverter control strategies, conventional linear approaches are predominantly employed for basic regulation [12]–[14]. While these methods ensure stable steady-state operation, their dynamic performance is often constrained by conservative bandwidth settings required for stability and decoupling, leading to sluggish responses during transient events [15]. Furthermore, attempting to mitigate these limitations by augmenting the controllers with additional compensation networks (such as virtual inertia and damping loops) inevitably increases the system order, potentially compromising stability margins and introducing oscillation risks under specific grid conditions [14].

Nonlinear control methods typically include deep reinforcement learning [16]–[18], hysteresis control [19]–[21] and sliding mode control [22], [23]. To address model parameter

This work was supported in part by the National Natural Science Foundation of China under Grant 52207106 and in part by the Fundamental Research Funds for the Central Universities under Grant 2025ZYGXZR026 and in part by the Key-Area Research and Development Program of Heilongjiang Province under Grant 2024ZX08C05. (Corresponding author: Kaishun Xiahou).

Zhijun Zeng, Kaishun Xiahou, Yang Liu, Chuanyue Li and Q. H. Wu are with the School of Electric Power Engineering, South China University of Technology, Guangzhou 510641, China. (e-mail: xiahouks@scut.edu.cn)

Lei Wang is with the School of Shipping and Maritime Studies, Guangzhou Maritime University, Guangzhou 510700, China.

Jun Liang is with the School of Engineering, Cardiff University, Cardiff, CF24 3AA, UK.

dependence, deep reinforcement learning approaches are increasingly studied. While avoiding complex explicit physical models, they face challenges in designing reward functions and weighting multi-objective criteria. Hysteresis and sliding mode controls offer implementation ease and robustness but suffer from non-fixed switching frequencies and sensitivity to initial parameters. For example, the direct power regulation strategy for GCIs in [24] provides strong robustness, disturbance rejection capability and freedom from model dependence. However, its variable switching frequencies still complicate filter design.

Distinct from these traditional nonlinear strategies, model predictive control (MPC) offers superior fast dynamic response and robust disturbance rejection [25]–[28]. Theoretically, MPC uses a dynamic model to predict system behavior. Although MPC can inherently handle nonlinearities, much of its application to power converters relies on averaged-value models to reduce computational burden. While valid for system-level studies, this approach introduces two practical challenges. First, when high-fidelity control is required, the mismatch between the averaged model and the actual switched system can cause suboptimal performance and increased switching losses. Second, using more detailed models increases computational complexity, and non-deterministic computation time leads to variable switching frequencies, complicating output filter design. Alternatively, data-driven methods have been actively explored to address model dependency in conventional control strategies, including MPC [29], [30], by leveraging operational data to reduce the need for precise system modeling.

Conventional linear and nonlinear control methods suffer from sluggish dynamics, variable switching frequencies, and PLL-dependent instability. To bridge this gap, this paper proposes an energy control (EC) strategy based on energy balance principles. This approach simultaneously achieves fast transient response without complex transformations, maintains a fixed switching frequency for simplified filtering, and enables PLL-free synchronization by directly governing instantaneous energy flow. The contributions of this paper are as follows:

(1) An EC strategy is proposed for both the bidirectional DC/DC converters (BDCs) in the BESS and the GCIs in the PV system of the microgrid. The EC strategy has the advantage of a fixed switching frequency, which facilitates the filter design. Besides, a dual-buck modulation scheme is designed for EC to prevent direct shoot-through faults in pulse width modulation.

(2) Without employing coordinate transformations, the EC strategy achieves power decoupling and enables seamless grid connection. Compared with traditional decoupling control and PLL-based synchronization, it significantly enhances the dynamic response of the system by eliminating the need for coordinate transformation and linear tracking methods.

(3) A phase compensation method independent of circuit parameters is proposed, with phase compensation components subsequently added to the controller, thus effectively mitigating the phase shift caused by inherent circuit impedance.

(4) An improved EC with data-driven compensation (EC-DDC) is developed to facilitate controller parameter selection. Furthermore, a sequential quadratic programming (SQP) optimizer is integrated in parallel with the regression model to enhance parameter optimization. The proposed EC-DDC demonstrates enhanced power quality metrics, thereby confirming the feasibility and effectiveness of the proposed approach.

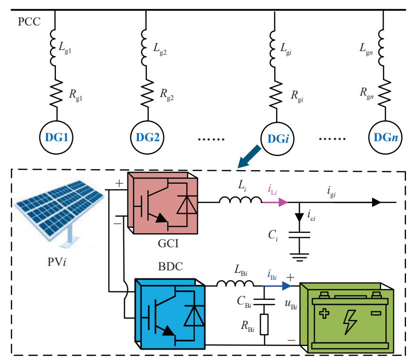

Fig. 1: Topology of PV-battery AC microgrid.

II. Modeling and Energy Controller Design for PV-Battery Power Converters

A. Modeling of PV-battery Microgrid

This paper focuses on the AC microgrid composed of n distributed generators (DGs) with the same topology. Each DG unit incorporates a BESS with a BDC and a PV system with a GCI, where the DC buses of the BDC and GCI share a common connection, as depicted in Fig. 1. The detailed models are described as follows.

1) BDC Model: The model of the BDC in the i-th DG is expressed as

$$\begin{cases} L_{\mathrm{B}i}\dfrac{di_{L\mathrm{B}i}(t)}{dt} = s_{\mathrm{B}i}(t)\,U_{ini} - u_{\mathrm{B}i}(t) - i_{L\mathrm{B}i}(t)\cdot R_{\mathrm{B}i} \\ C_{\mathrm{B}i}\dfrac{du_{\mathrm{B}i}(t)}{dt} = i_{L\mathrm{B}i}(t) - i_{\mathrm{B}i}(t) \end{cases} \tag{1}$$

where $L_{\mathrm{B}i}$ ($i = 1, 2, ..., n$) and $C_{\mathrm{B}i}$ represent the inductance and the capacitance of the i-th BDC, respectively. $R_{\mathrm{B}i}$ is the series resistance of the battery capacitor. $i_{\mathrm{LB}i}$ and $i_{\mathrm{B}i}$ denote the inductor current and the output current, respectively. $U_{\mathrm{in}i}$ and $u_{\mathrm{B}i}$ denote the DC input voltage and the battery voltage, respectively. $s_{\mathrm{B}i} \in \{0, 1\}$ is the switching function that determines the state of the upper switch. $s_{\mathrm{B}i} = 1$ corresponds to the high-frequency state, and $s_{\mathrm{B}i} = 0$ indicates the off state.

2) GCI Model: The GCI model in the i-th DG is given as

$$\begin{cases} L_i\dfrac{di_{Li}(t)}{dt} = s_{ij}(t)\,U_{ini} - u_{ci}(t) \\ C_i\dfrac{du_{ci}(t)}{dt} = i_{Li}(t) - i_{gi}(t) \end{cases} \tag{2}$$

where L_i and C_i refer to the inductance and the capacitance of the i-th GCI, respectively. $i_{\mathrm{L}i}$ and i_{gi} are the inductor current of inverters and the grid current, respectively. $s_{ij} \in \{0, 1\}$ is the switching function of the upper switch of the i-th GCI, where $j \in \{1, 2\}$ denotes the j-th converter arm. $s_{ij} = 1$ corresponds to the high-frequency state of the upper switch of the j-th arm, and $s_{ij} = 0$ indicates the off state. It is worth noting that while digital implementation inevitably

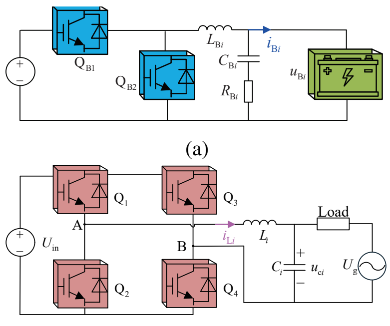

(a)

(b)

Fig. 2: Topology of (a) BDC and (b) GCI.

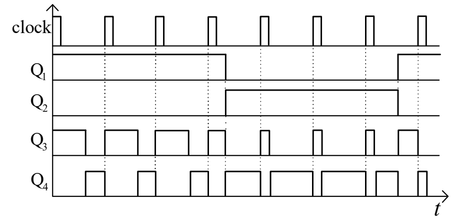

Fig. 3: Schematic diagram of switch pulse signals.

introduces time delays, the proposed control strategy exhibits strong robustness against such latencies. Extensive simulations incorporating time delays demonstrate negligible impact on both dynamic response and total harmonic distortion (THD) performance. For brevity, these comparative results are provided in the supplementary material associated with this submission, confirming the validity of the simplified model used herein for clarity.

B. Energy Controller Design for Power Converters

To overcome the limitations of existing control paradigms, the proposed EC strategy shifts the control objective from tracking references to maintaining instantaneous energy balance. This fundamental shift achieves fast dynamic response, fixed switching frequency, and PLL-independent operation, as detailed in the subsequent sections.

1) Dual-buck Modulation Scheme of Power Converters: Traditional modulation methods risk both switches in the bridge arm operating simultaneously at high frequency within the same switching period, causing direct short-circuits that may damage switching devices or induce a serious failure [31]. This paper employs a dual-buck modulation scheme to circumvent these issues for power converters.

For the BDC shown in Fig. 2(a), $\mathrm{Q_{B1}}$ operates at high-frequency switching with $\mathrm{Q_{B2}}$ closed during charging, while $\mathrm{Q_{B2}}$ operates at high-frequency switching with $\mathrm{Q_{B1}}$ off during discharging. The GCI in Fig. 2(b) adopts a similar strategy and the switching pulse signals are shown in Fig. 3. For the positive current, $\mathrm{Q_1}$ conducts constantly and $\mathrm{Q_2}$ is off. $\mathrm{Q_3}$ and $\mathrm{Q_4}$ switch at high-frequency. For the negative current, $\mathrm{Q_1}$ is off and $\mathrm{Q_2}$ conducts constantly, while $\mathrm{Q_3}$ and $\mathrm{Q_4}$ continue to switch at high-frequency. Compared with conventional modulation, this approach reduces high-frequency switching in one phase.

2) Instantaneous Power of GCI: According to the instantaneous power theory, the amplitude of the active power and the reactive power can be expressed as

$$P = S\cos\omega t, Q = S\sin\omega t \tag{3}$$

where S is the instantaneous power under the rotating coordinate frame. P and Q are the in-phase part and the orthogonal part, respectively. ω is the angular frequency of the grid voltage.

Inspired by (3), P can be expressed by multiplying a unit sine wave that is in-phase with the grid voltage by a coefficient. The in-phase unit sine wave u_p can be derived by dividing the grid voltage by its amplitude. The orthogonal unit sine wave u_q is obtained by shifting u_p 90 degrees. The coefficients mentioned above can be determined as

$$a_\mathrm{p} = U_\mathrm{g} i_\mathrm{p}, a_\mathrm{q} = U_\mathrm{g} i_\mathrm{q} \tag{4}$$

where a_p and a_q are the coefficients, respectively. U_g is the amplitude of the grid voltage. i_p and i_q are the active current reference and the reactive current reference, respectively.

Unlike traditional PLL-based methods, the proposed EC strategy implements a self-synchronization mechanism centered on the direct generation of the unit sine wave signals u_p and u_q. Specifically, the instantaneous grid voltage at the point of common coupling is monitored, and its fundamental amplitude is estimated in real time via a sliding-window amplitude estimator. A unit sine wave synchronized with the grid voltage is then derived through algebraic normalization, and the orthogonal signal u_q is obtained by shifting u_p by $90°$. This approach eliminates the need for PLL design and tuning while maintaining robustness under small grid disturbances. Consequently, the dynamic response is limited only by the latency of the amplitude estimation, enabling fast and accurate power control. Finally, the output power in natural coordinate frame is given as

$$\mathcal{S} = a_\mathrm{p} u_\mathrm{p} + a_\mathrm{q} u_\mathrm{q}. \tag{5}$$

In practice, adjusting Eq. (4) generates the required real-time reference power. This represents a grid frequency sine wave, as established. Consequently, the output current direction of the inverter is determined by the sign of the term in Eq. (5). Under ideal conditions, the switching combination of the GCI changes with its sign, enabling precise output control.

3) Operation Principle of Power Converters: In any switching period nT_s, both the BDC and the GCI can be represented by

$$W_\mathrm{in}(n) = W_\mathrm{out}(n) + \Delta W_\mathrm{c}(n) + \Delta W_\mathrm{l}(n) \tag{6}$$

where W_in and W_out are the input and output energies, respectively. $\Delta W_\mathrm{c}(n)$ and $\Delta W_\mathrm{l}(n)$ are the energy changes of the capacitor and the inductor, respectively.

a) EC of BDC: Assuming all components are ideal, the equivalent circuit behaves as a buck converter during the charging mode. In the discharging mode, the equivalent circuit functions as a boost converter. The control objective in both modes is to maintain the output voltage equal to a specified voltage value. Since the capacitor voltage equals the battery

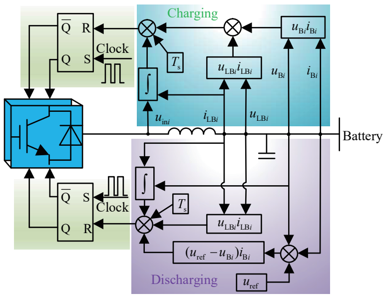

Fig. 4: Control diagram of BDC.

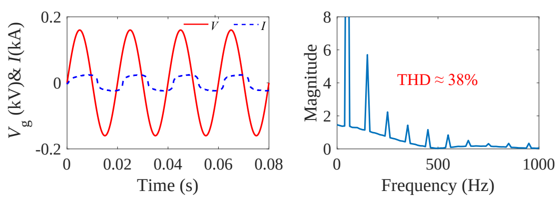

Fig. 5: Simulation results of GCI under conventional EC.

voltage and remains constant in both modes, the term $\Delta W_c(n)$ in (6) equals to 0. Then

$$W_{\text{in}}(n) = W_{\text{out}}(n) + \Delta W_1(n). \tag{7}$$

From Eq. (7), the control equation of the charging mode is expressed by

$$\int_0^{DT_s} u_{\text{ini}} i_{\text{LB}i} \text{d}t = u_{\text{B}i} i_{\text{B}i} T_s + u_{\text{LB}i} i_{\text{LB}i} T_s. \tag{8}$$

The control equation of the discharging mode is represented as

$$\int_0^{DT_s} u_{\text{B}i} i_{\text{LB}i} \text{d}t = (u_{\text{ref}} - u_{\text{B}i}) i_{\text{B}i} T_s + u_{\text{LB}i} i_{\text{LB}i} T_s \tag{9}$$

where u_{ref} and $u_{\text{LB}i}$ represent the DC-side voltage and the inductor voltage, respectively. D is the duty ratio. The specific control block diagram of the BDC is shown in Fig. 4.

In Eqs. (8) and (9), the control variables are the battery voltage u_{B} and the DC voltage u_{ref}, respectively, and the rest are all measured quantities. At the beginning of each cycle, the control reference values need to be calculated in advance and remain constant throughout this entire cycle. At the start of each switching cycle, the integrator begins operation. When the output value of the integrator reaches the output reference value, the controller transmits a signal to shut off the switch. Then, the integrator persists in its operation and does not reset to zero until the rising edge of the next switching cycle. Subsequently, this process is reiterated.

b) EC of Single-phase GCI: The detailed expression of Eq. (6) in the GCI is

$$\int_0^{DT_s} u_{\text{ab}i}\, i_{\text{L}i}\, \text{d}t = \mathcal{S}T_s + u_g C_i \dot{u}_g T_s \tag{10}$$

where $u_{\text{ab}i}$ indicates the voltage between A and B. u_g represents the grid voltage. The application is similar to that of the BDC and will not be elaborated here. The only difference is that in Eq. (10), the integrator resets immediately after the turn-off signal appears and remains at zero until the next pulse signal appears. However, the controller designed based on Eq. (10) still exhibits deficiencies and requires further improvement, as detailed below.

III. POWER QUALITY IMPROVEMENT BASED ON DATA-DRIVEN COMPENSATION

Fig. 5 displays the output current waveform of the EC-controlled GCI derived from Eq. (10), revealing a phase shift and harmonic distortion caused by AC system nonlinearities. To address these issues, a DDC method is proposed for power quality improvement. The GCI controller structure and the flowchart of the SQP optimizer are illustrated in Fig. 6(a) and (b), respectively. Details are provided below.

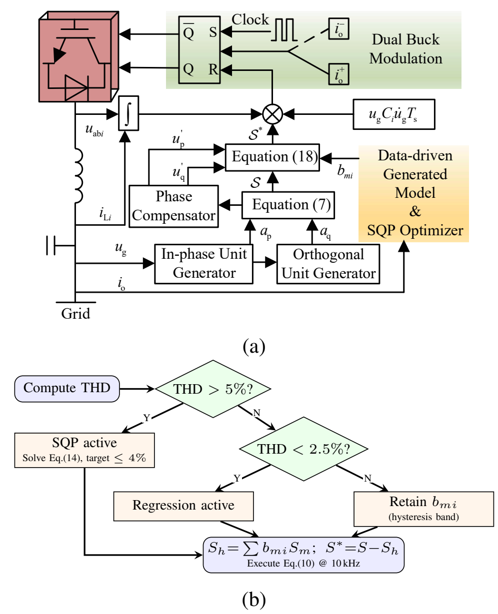

(a)

(b)

Fig. 6: (a) Energy control with data-driven compensation for GCI, (b) Flowchart of the SQP optimizer.

A. Phase Detection and Compensation

In this paper, it is feasible to compensate the current directly. The unit power output is taken as the standard value. Therefore, the precise phase of the output current can be expressed as

$$\varphi_c = \varphi_{\text{io}} - \varphi_{\text{iref}} \tag{11}$$

where φ_c is the compensation angle for the reference current. φ_{io} and φ_{iref} are the angles of the output current and the reference current, respectively. Consequently, the output current phase is determined simply by adjusting u_p and u_q to u_p' and u_q', respectively. The proposed phase compensation method is inherently robust to grid frequency fluctuations. The compensation angle φ_c is calculated in real time based on the instantaneous phase difference between the measured output current and its reference. Since both the reference current and the measured output current are equally affected by grid frequency deviations, their relative phase error remains largely unchanged. This error-driven mechanism ensures accurate phase tracking regardless of slow variations in the fundamental grid frequency, without relying on a fixed nominal frequency value.

B. Harmonic Elimination

By performing Fourier analysis on the output current, it is found that the output current is dominated by odd harmonics. Since $\mathcal{S}$ is a standard sine wave with the same frequency as the power grid, power quality can be improved by injecting odd harmonics in phase with $\mathcal{S}$ into the output current with opposite polarity. The odd harmonic power can be expressed as

$$\mathcal{S}_{\mathrm{h}} = \sum_{m=3,5,7\cdots} b_{mi}\mathcal{S}_m \tag{12}$$

where $\mathcal{S}_{\mathrm{h}}$ and $\mathcal{S}_m$ are the total power of odd harmonics and the power of a single harmonic, respectively. b_{mi} is the coefficient. The expression of $\mathcal{S}_m$ is similar to Eq. (5), except that it represents the power of the odd-order harmonic with an amplitude of one. Thus, the harmonic power level is only determined by b_{mi}. To obtain the desired compensation, a DDC method is employed. The controller initially collects output current data containing odd-order harmonic amplitudes under various steady-state operating points through online monitoring to compile a dataset. Subsequently, offline processing is implemented to establish an input-output mathematical relationship. This constructed nonlinear mathematical model is then integrated into the compensation loop. The control system can select the corresponding b_{mi} based on this model under different conditions, thereby forming a real-time control system.

1) Data Acquisition and Preprocessing: For control simplification under unit power factor operation, the parameter a_{q} in Eq. (5) is typically set to zero, with the output current phase angle being determined by Eq. (10). With the grid voltage and circuit parameters held constant, data are collected by sweeping a_{p} from 8 to 40 in increments of 0.1. Three cycles of output current are recorded per setting. During transient states, the output current waveform exhibits significant distortion. To ensure accurate harmonic analysis, the first cycle is excluded from spectral evaluation, and only the subsequent two stable cycles are analyzed. Harmonic characterization employs only the latter two cycles via Fourier analysis to extract odd harmonic amplitudes. This study considers the first six odd-order harmonics (excluding the fundamental), yielding a 321×6 feature matrix representing harmonic amplitude variation across parameter configurations.

2) Model Regression and Validity Verification: In an idealized setting with only a single independent variable, the mathematical model is typically formulated as a single-variable polynomial regression. A standard regression formulation is selected as

$$f(x) = \sum_{k=0}^{N} h_k x^k \tag{13}$$

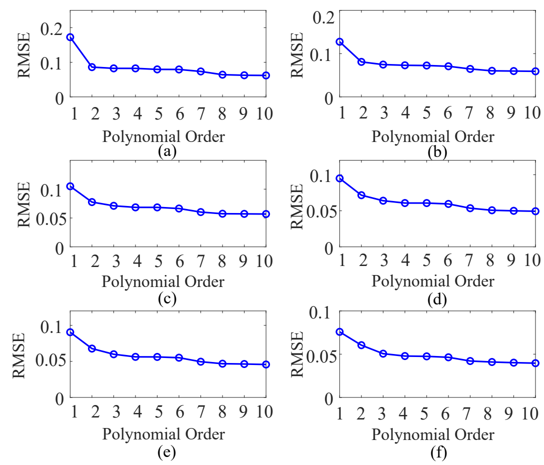

Fig. 7: RMSE values of the regression model of (a) 3rd-order ; (b) 5th-order; (c) 7th-order; (d) 9th-order; (e) 11th-order and (f) 13th-order harmonics.

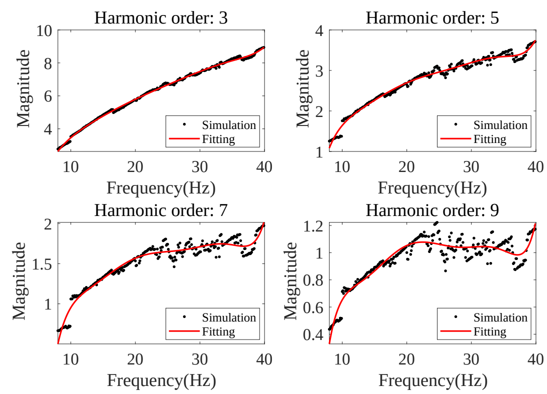

Fig. 8: Harmonic model for parameter selection.

where h_k is the polynomial coefficient. Fig. 7 shows that the average RMSE for the six models is less than 0.08 when $k = 7$, confirming satisfactory results. Thus, a 7th-order univariate polynomial is selected as the optimal nonlinear regression model. Fig. 8 presents the regression models for the 3rd, 5th, 7th, and 9th order harmonics. The fitting models for the 11th and 13th order harmonics are not explicitly shown due to their minimal variations compared to previous orders. In practical applications, the parameters can be selected based on the variation trends of the models across harmonic orders.

3) Dynamic Optimization of Parameters: An SQP-based optimizer is incorporated into the regression model to further improve the power quality. The optimization model is represented as

$$\begin{aligned} \min_{b_{mi}} \quad & \left| I_{\mathrm{g}i}(b_{mi}) - \sqrt{a_{\mathrm{p}}^2 + a_{\mathrm{q}}^2} \right| \\ \text{s.t.} \quad & \mathrm{THD}(b_{mi}) \leq 4\% \\ & 0 \leq b_{mi} \leq \sqrt{a_{\mathrm{p}}^2 + a_{\mathrm{q}}^2} \end{aligned} \tag{14}$$

where $\mathrm{THD}(b_{mi})$ is the harmonic of the output current. As illustrated in Fig. 6(b), the coefficients b_{mi} are updated once per grid cycle and held constant within each cycle. A three-zone hysteresis governs the SQP activation: (1) for $\mathrm{THD} \leq 2.5\%$, the regression output is used directly; (2) for $2.5\% < \mathrm{THD} \leq 5\%$, the current parameters are retained;

(3) for THD $>5\%$, persisting for two consecutive cycles, the SQP is activated by using the regression output as the initial guess to solve Eq. (14) and reduce THD to below 4%. After convergence, the operating point falls within the hysteresis band, and re-activation requires THD to exceed 5% again, thereby preventing chattering. The SQP terminates upon reaching the preset maximum iteration count, and the iteration yielding the lowest THD is selected as the final output. Since the SQP employs monotonic descent from the regression initial point, performance is guaranteed to be no worse than the regression model alone. Extension to severe grid distortion beyond the regression design envelope will be investigated in future work.

4) Total Reference Power Estimation: Combining Eq. (5), Eq. (12) and the result of Eq. (14), the total reference control power is given by

$$\mathcal{S}^* = \mathcal{S} - \mathcal{S}_{\mathrm{h}}. \tag{15}$$

The final control equation can be obtained by replacing $\mathcal{S}$ in Eq. (10) with Eq. (15). Furthermore, the proposed DDC loop is capable of suppressing odd-order harmonics, thereby compensating for distortions induced by dead-time effects and forward voltage drops. Consequently, the nonlinearity typically associated with the current zero-crossing region is inherently mitigated by this mechanism.

C. Stability Analysis

The stability of the proposed EC strategy is analyzed using the Lyapunov direct method. The BDC in charging mode is selected as the representative case due to its structural similarity. Since both the BDC and GCI share the same system matrix structure, and the energy-based duty ratio update law ensures global asymptotic stability regardless of topology, proving the stability of the BDC is sufficient to establish the theoretical foundation of the EC method.

The inductor only transfers energy and does not consume it in any switching cycle according to the volt-second balance, when the converter operates in a steady-state condition. Therefore, the expression of duty ratio can be obtained as

$$D(n) = \frac{u_{\mathrm{Bref}i} i_{\mathrm{B}i}(t)}{u_{\mathrm{in}i}(t) i_{\mathrm{LB}i}(t)} \tag{16}$$

where $D(n)$ is the duty ratio in the n-th switching cycle, and $u_{\mathrm{Bref}i}$ is the reference output voltage of the i-th battery. The BDC in charging mode can be expressed by

$$\dot{x}(t) = Ax(t) + Bu_{\mathrm{in}}(t) \tag{17}$$

where $x(t)$ is the state vector and can be expressed as $x(t) = [i_{\mathrm{LB}i}(t);\ u_{\mathrm{B}i}(t)]$, $A = [-R_{\mathrm{L}}/L,\ -1/L;\ 1/C,\ -1/(RC)]$, $B = [D/L;\ 0]$. R_{L} is the parasitic resistance of the inductor, which can be neglected for simplicity. Applying a disturbance to Eq. (17) will simultaneously cause perturbations in the output voltage, inductor current and duty ratio. Here, the perturbations are denoted by $\hat{u}_{\mathrm{B}i}(t)$, $\hat{i}_{\mathrm{LB}i}$ and $\hat{D}$. Accordingly, Eq. (16) and Eq. (17) are written as

$$\hat{D}(n) = \frac{U_{\mathrm{Bref}i}}{RU_{\mathrm{in}i} I_{\mathrm{LB}i}} \hat{u}_{\mathrm{B}i}(t) - \frac{D}{I_{\mathrm{LB}i}} \hat{i}_{\mathrm{LB}i}(t) \tag{18}$$

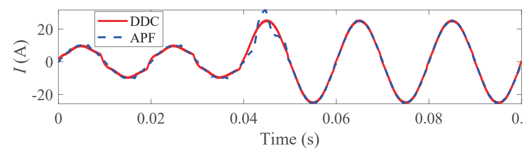

Fig. 9: Simulation results of output current.

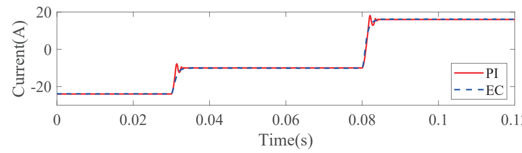

Fig. 10: Dynamic response of battery current.

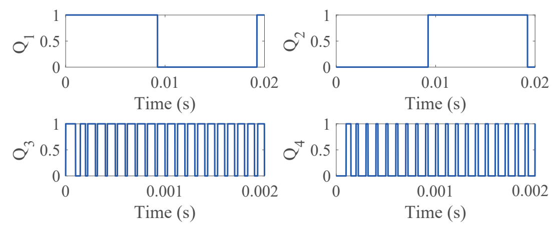

Fig. 11: Pulse signals of GCI under EC-DDC.

$$\dot{\hat{x}}(t) = A\hat{x}(t) + B_1 U_{\mathrm{in}} \tag{19}$$

where the capital letters without hat label represent the steady-state quantities. Besides, $\hat{x}(t) = \left[\hat{i}_{\mathrm{LB}i}(t); \hat{u}_{\mathrm{B}i}(t)\right]$ and $B_1 = \left[\hat{D}\big/L; 0\right]$. Define a Lyapunov function

$$V_{\mathrm{L}} = \frac{1}{2} L \hat{i}_{\mathrm{LB}i}^2 + \frac{1}{2} C \hat{u}_{\mathrm{B}i}^2. \tag{20}$$

Combining Eq. (18) and Eq. (20), the derivative of V_{L} becomes

$$\dot{V}_{\mathrm{L}} = -R\hat{i}_{\mathrm{LB}i}^2 - \frac{\hat{u}_{\mathrm{B}i}^2}{R} - \frac{\hat{D}^2 I_{\mathrm{LB}i}}{D} + \frac{U_{\mathrm{Bref}i}\hat{u}_{\mathrm{B}i}\hat{D}}{RD}. \tag{21}$$

In this steady-state system, an incremental disturbance in the output voltage inevitably leads to a decrease in duty ratio. Conversely, any decrement disturbance in the output voltage will result in an increase in duty ratio. This implies that under any disturbance, $\hat{u}_{\mathrm{B}i}$ and $\hat{D}$ always have opposite signs, making the last term of Eq. (21) always less than 0. In conclusion, the system is stable.

IV. Simulation Studies

Simulation studies were conducted on the PV-battery microgrid in Fig. 1 with three DGs to demonstrate the advantages of the proposed method. All batteries share the same charging-discharging principle; thus, the simulation focuses on a single BDC unit. PV1 operates in MPPT mode, PV2 and PV3 adjust their output to match the received power command. Simulations focused on comparing the performance of a PV-battery microgrid system using the proposed method with that using conventional PI control. The specific system parameters are $L_1 = L_3 = 6.6$ mH, $L_2 = 3.3$ mH. $C_1 = C_3 = 80$ μF, $C_2 = 120$ μF. The switching frequency of the BDC and the GCI is 10 kHz, and the nominal frequency of power grid is 50 Hz.

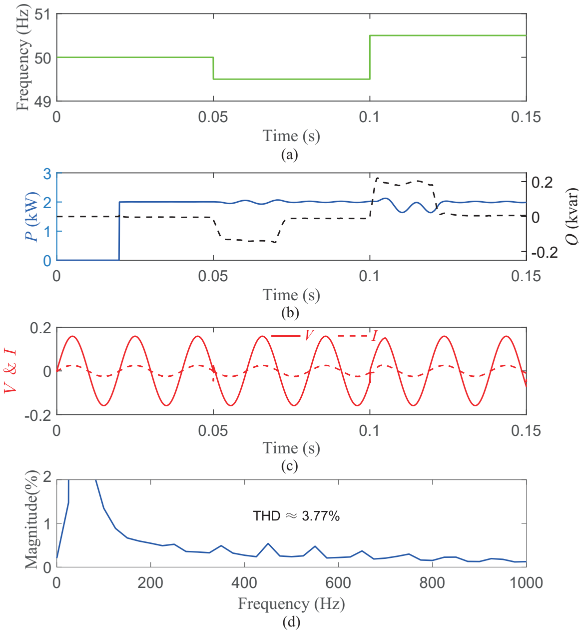

Fig. 12: Simulation results under grid frequency fluctuations. (a) Frequency; (b) P and Q; (c) Grid voltage and output current; (d) Harmonic spectrum of current.

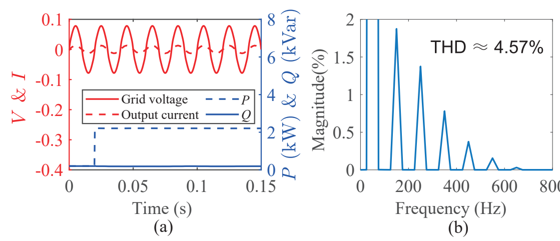

Fig. 13: Simulation results under grid harmonic background. (a) Grid voltage, output current, P and Q; (b) Harmonic spectrum of grid voltage.

A. Comparison with Active Power Filtering

In this case, the harmonic compensation performance of the DDC is evaluated under severe grid distortion conditions and compared against an active power filter (APF). Initially, the system operates without compensation, resulting in a severely distorted current waveform. At $t = 0.04$ s, both the APF and DDC are activated simultaneously to mitigate the harmonics.

As shown in Fig. 9, the DDC method demonstrates superior dynamic performance with faster convergence and less overshoot than the APF. Although both approaches achieve similar steady-state accuracy, DDC provides a distinct industrial advantage. Unlike APFs requiring additional hardware, DDC relies solely on embedded control algorithms in the existing inverter, reducing cost and volume while maintaining high performance.

B. Dynamic Performance of Battery Current

In this case, the current performance of the battery is evaluated under step changes of reference value. The battery is initially charged at a constant current of 23 A. At $t = 0.03$ s, the charging current changes to 10A. At $t = 0.08$ s, the battery shifts to a discharge state with a constant current of 15 A.

Fig. 10 shows a comparison of the charging and discharging currents for BESS under the proposed EC and PI method. Clearly, the proposed method eliminates overshoot during charging-discharging transitions and current variations. Examination of magnified current plots within identical time windows confirms the EC achieves specified currents faster. This conclusively demonstrates inherent overshoot suppression and superior dynamic performance of the EC. These advantages enhance the stability of the BESS when encountering disturbances. Then, the pulse signals are presented exclusively in Fig. 11. These results validate the theory presented in Fig 3. Furthermore, by significantly reducing the high-frequency switching of two switches in the bridge arm, the dual-buck modulation effectively reduces the risk of direct shoot-through and also minimizes energy losses.

C. Robustness under Grid Disturbances

To comprehensively evaluate the robustness of the proposed system under non-ideal grid conditions, a series of tests were conducted covering grid frequency fluctuations and operation under harmonic backgrounds. Grid frequency stability is crucial for synchronization and power control. In Fig. 12, the grid frequency undergoes significant step changes from 50 Hz to 49.5 Hz at $t = 0.05$ s, rises to 50.5 Hz at $t = 0.1$ s. As illustrated in Fig. 12(a) and (b), despite these frequency perturbations, the P and Q remain stable and track their reference values accurately. The transient impact on power output is minimal, demonstrating effective decoupling between power regulation and grid frequency. Furthermore, Fig. 12(c) shows that the output current maintains a high-quality sinusoidal waveform and remains synchronized with the grid voltage throughout the frequency transitions. The harmonic performance is analyzed in Fig. 12(d), where the THD of the output current is approximately 3.77%. These results confirm that the EC-DDC strategy ensures reliable operation and high power quality even when the grid frequency deviates by ± 0.5 Hz.

Then, to evaluate the immunity of the control strategy to grid voltage distortion, the system was tested under a grid background containing predefined harmonics. A THD of approximately 3.4% was intentionally injected into the grid voltage source at $t = 0.08$ s, which can be seen in Fig. 13(a). The performance of the system under non-ideal grid condition is presented in Fig. 13(b). The results demonstrate stable and periodic operation after an initial transient period around 0.05 seconds. The active and reactive power outputs maintain their setpoints with minimal oscillation. More importantly, the output current waveform remains synchronized with the distorted grid voltage, preserving the required phase relationship. In this case, the THD of the output current is adopted as the metric for assessing steady-state performance. The calculated THD of the output current is 3.4%. This indicates that the proposed control scheme effectively rejects harmonic interference from the grid, ensuring stable power delivery and high-quality current injection even in the presence of background voltage distortion.

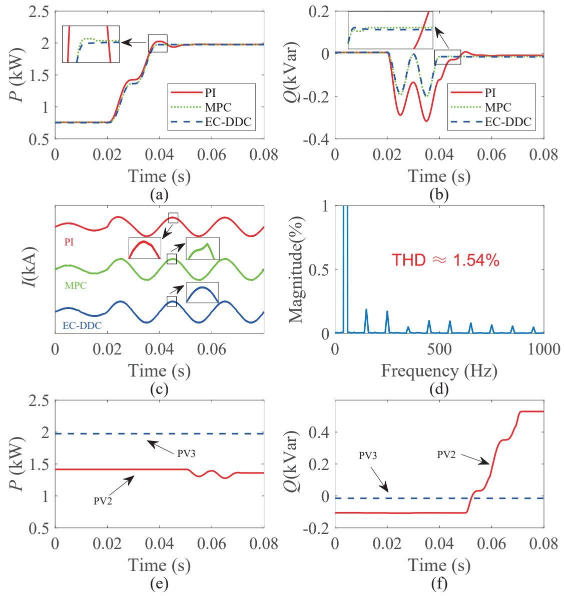

Fig. 14: Simulation results of DG1 operating in the MPPT mode. (a) P (b) Q; (c) Output current; (d) Harmonic spectrum of current under EC-DDC; (e) P under EC-DDC; (f) Q under EC-DDC.

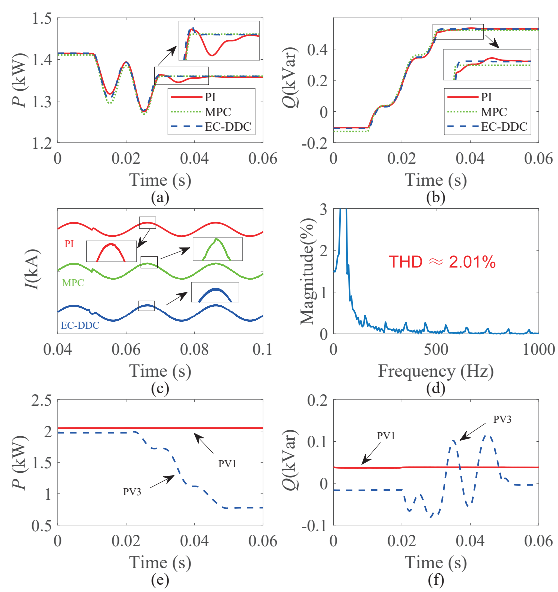

Fig. 15: Simulation results of DG2 operating in direct control mode. (a) P; (b) Q; (c) Output current; (d) Harmonic spectrum of current under EC-DDC; (e) P under EC-DDC; (f) Q under EC-DDC.

D. Dynamic Performance under MPPT Mode

The reference current variation caused by solar array irradiance variation in MPPT mode is simulated. The perturbation observation method is used in MPPT. In the simulation, the initial irradiance is set to 226 $\mathrm{W/m^2}$. Subsequently, the irradiance increases to 600 $\mathrm{W/m^2}$ at $t = 0.02$ s. Initially, the control parameters b_{mi} of the energy controller are $b_{31} = 1.8$, $b_{51} = 0.32$, $b_{71} = 0.075$, $b_{91} = 0.0035$, $b_{111} = b_{131} = 0$, respectively. With the change of irradiance, the parameters change to $b'_{31} = 4.72$, $b'_{51} = 0.84$, $b'_{71} = 0.197$, $b'_{91} = 0.009197$, $b'_{111} = b'_{131} = 0.0001$.

The comparative performance of the PI, MPC and the proposed EC-DDC strategies is visually presented in Fig. 14(a)-(f) and summarized quantitatively in Table I. Following an irradiance step increase, the PI controller exhibits significant overshoot and sustained oscillations in active power as shown in Fig. 14(a), accompanied by noticeable reactive power coupling depicted in Fig. 14(b) and distorted current transients rich in high-frequency harmonics observed in Fig. 14(c). In contrast, while MPC reduces overshoot and improves decoupling, it still introduces minor ripples in both active and reactive power. The EC-DDC method achieves the smoothest and fastest transition with negligible overshoot, minimal reactive power deviation, and a high-fidelity sinusoidal output current. This is confirmed by a measured THD of only 1.54% as illustrated in Fig. 14(d). Moreover, Fig. 14(e) and Fig. 14(f) show that the transient event in one distributed generator does not affect the power outputs of the other two generators, confirming system-level stability and modularity. These qualitative observations align with the quantitative metrics in Table I where the EC-DDC consistently achieves the lowest ΔP, ΔQ, settling time Δt, and THD among all methods under MPPT operation.

E. Dynamic Performance under Direct Control Mode

To further validate the dynamic decoupling capability and response speed of the proposed control strategy, a test was conducted for the DG2 operating in direct control mode. The initial operating point was set to an active power of 1442 W and a reactive power of -118 Var. At $t = 0.01$ s, a step change was applied to the reactive power reference, increasing it to 540 Var. The parameters of the energy controller were configured for this scenario, with initial values of $b_{32} = 3.1$, $b_{52} = 0.63$, $b_{72} = 0.13$, $b_{92} = 0.006$, $b_{112} = b_{132} = 0$. These parameters were then adaptively adjusted to $b'_{32} = 3.11$, $b'_{52} = 0.575$, $b'_{72} = 0.165$, $b'_{92} = 0.008$, $b'_{112} = b'_{132} = 0.0001$ in response to the power reference change.

The comparative transient responses of the PI, MPC, and EC-DDC controllers are presented in Fig. 15. Fig. 15(a) and (b) illustrate the active and reactive power responses, respectively. When the reactive power reference undergoes a step change, the PI controller induces significant and prolonged oscillations in active power, while MPC provides improved damping with reduced disturbance. Although EC-DDC exhibits a slight overshoot in active power, its dynamic response speed is comparable to that of MPC, and more importantly, it maintains excellent decoupling between active and reactive power control loops. As shown in Fig. 15(c), the output current under EC-DDC remains nearly sinusoidal throughout the transient, whereas noticeable distortion occurs near the current peaks under both PI and MPC control. The harmonic spectrum analysis in Fig. 15(d) confirms a THD of approximately 2.01% during steady-state operation. Furthermore, as demonstrated in Fig. 15(e) and (f), the power outputs of the other two DGs remain unaffected by the local transient, highlighting the system robustness and modularity. These results, together with the data in Table I, show that EC-DDC achieves the smallest active power deviation ΔP, the minimal reactive power fluctuation ΔQ, the second fast settling time Δt, and the lowest THD, confirming its superior performance in direct control mode for PV-battery systems.

TABLE I: Data results of three modes

	MPPT mode				Direct control mode				Grid-connected/islanded switching mode			
	ΔP	ΔQ	Δt	THD	ΔP	ΔQ	Δt	THD	ΔP	ΔQ	Δt	THD
PI	1292.86W	341.05Var	37.1ms	2.10%	162.93W	663.51Var	41.4ms	2.85%	1289.25W	251.65Var	45.9ms	2.57%
MPC	1240.20W	223.51Var	21.4ms	3.02%	175.24W	661.15Var	20.8ms	1.85%	1252.49W	210.27Var	26.5ms	1.18%
EC-DDC	1238.99W	198.72Var	18.2ms	1.54%	142.06W	657.92Var	21.2ms	2.01%	1241.50W	191.33Var	30.3ms	1.80%

TABLE II: Comparison Table

	Complexity	Number of variables	Computational load	PLL requirement	Dynamic time constant	THD	Efficiency
PI	Low	3	Low	Yes	≈41.3ms	≈2.51%	95.36%
MPC	High	6	High	Yes	≈22.9ms	≈2.0%	97.2%
EC-DDC	Medium	3	Medium	No	≈23ms	≈1.78%	97.64%

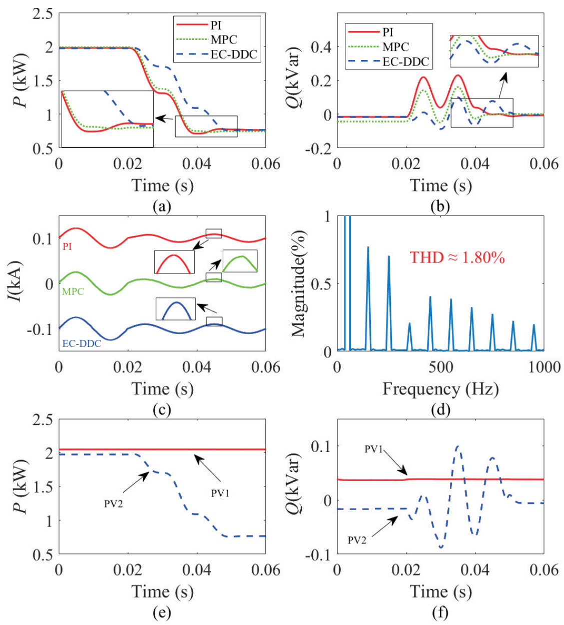

Fig. 16: Simulation results of DG3 under grid-connected to islanded switching conditions. (a) P; (b) Q; (c) Output current ; (d) Harmonic spectrum of current under EC-DDC; (e) P under EC-DDC; (f) Q under EC-DDC.

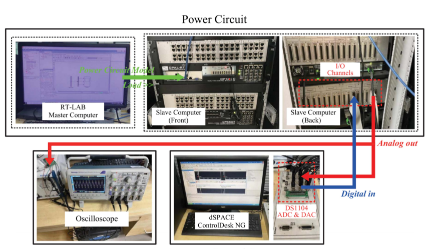

Fig. 17: Configuration of the experimental platform.

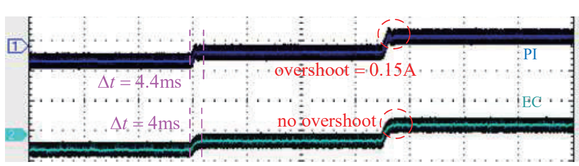

Fig. 18: Experimental results of the output current in BDC.

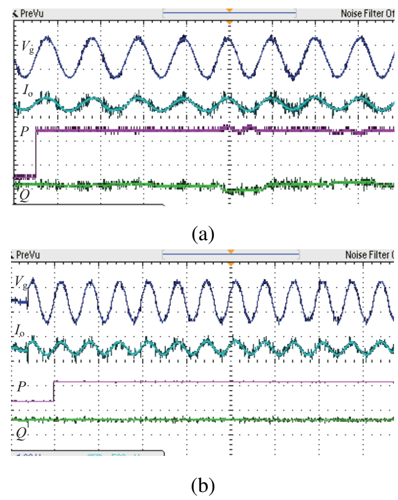

Fig. 19: Experimental results under grid disturbances. (a) Grid frequency fluctuations; (b) Harmonic backgrounds.

F. Grid-connected to Islanded Mode Switching

In this part, the primary objective is to demonstrate the power fluctuation performance of the control method during the transition from grid-connected to islanded operation. At $t = 0.02$ s, the connection to the main grid is severed, and DG3 transitions to islanded mode to independently supply a 770 W local load. The initial parameters are consistent with those of DG1 in Section V.A for grid-connected operation, while in islanded mode, all coefficients b_{mi} are set to zero to reflect the absence of grid support.

The comparative performance of the PI, MPC, and EC-DDC controllers during grid-connected to islanded mode switching is illustrated in Fig. 16 and summarized quantitatively in Table I. Fig. 16(a) shows that the PI controller suffers from prolonged oscillations and a slow return to steady state after the mode switch, while MPC reduces these fluctuations but still exhibits noticeable transients. In contrast, EC-DDC enables a smooth and stable transition with minimal power deviation. A similar trend is observed in reactive power, where EC-DDC achieves the smallest disturbance and quickest stabilization among the three methods as shown in Fig. 16(b). Although the dynamic response speed of EC-DDC is comparable to that of MPC, its output current remains highly sinusoidal throughout the transient in Fig. 16(d), unlike MPC, which shows peak

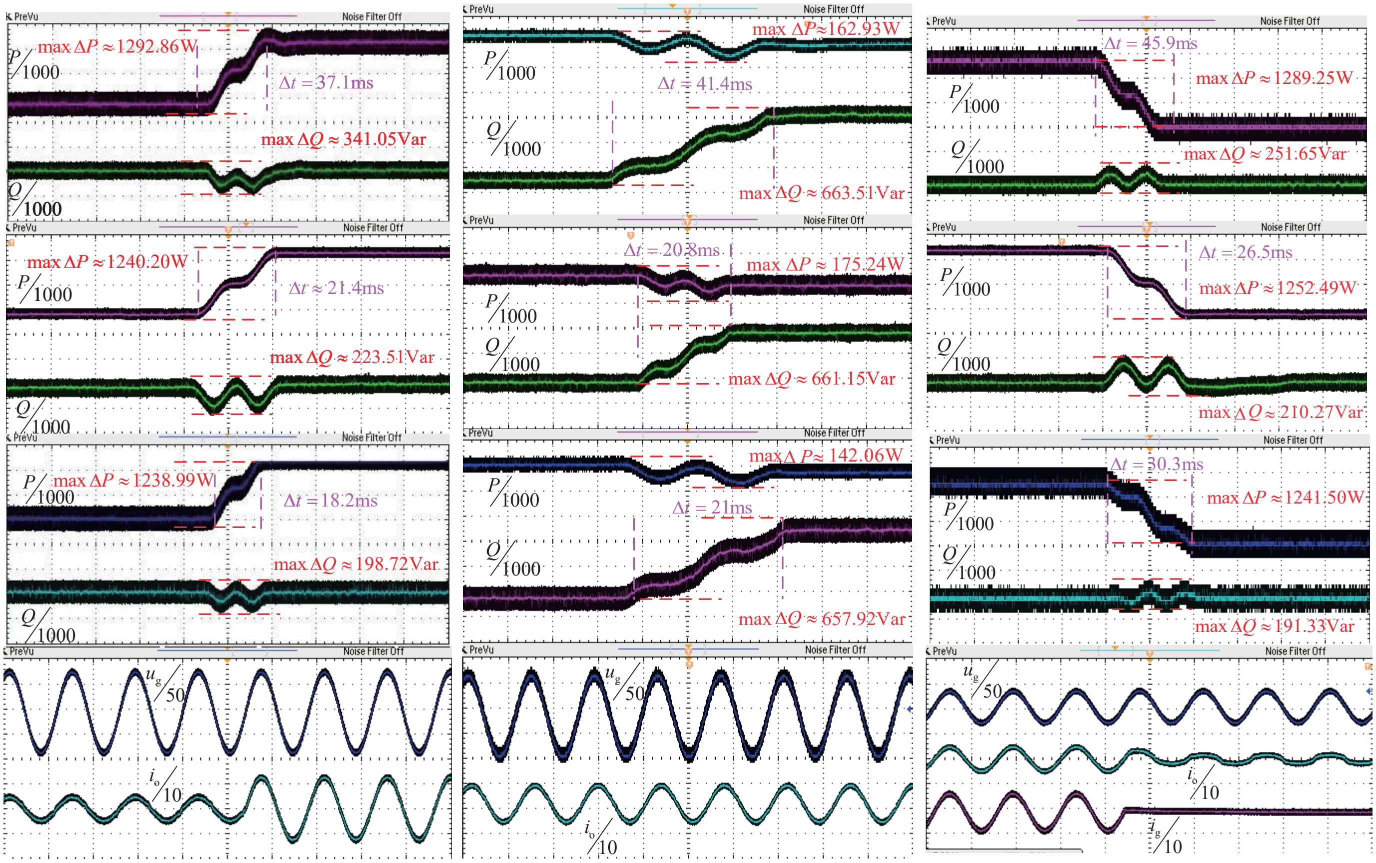

(a) (b) (c)

Fig. 20: Experimental results of the output current and power dynamic performance. (a) MPPT mode; (b) Direct control mode; (c) Grid-connected to islanded. (Top: power performance under PI control ; upper middle: power performance under MPC; lower middle: power performance under EC-DDC; bottom: grid voltage and output current).

distortion. The harmonic analysis in Fig. 16(d) confirms a low THD of approximately 1.8% under EC-DDC during islanded operation, matching the value reported in Table I. Fig. 16(e) and (f) further confirm that the transition of one DG does not impact the others, underscoring system modularity. Together with the quantitative metrics in Table I, which show that EC-DDC achieves the smallest active power deviation, the minimal reactive power fluctuation ΔQ, the lowest THD, and a settling time comparable to or better than existing methods, the results demonstrate the superior robustness and power quality of EC-DDC during mode transitions in PV-battery systems.

V. EXPERIMENT RESULTS

The microgrid is built on a real-time digital simulator platform OP5600 to verify the control performance of EC, which is shown in Fig. 17. The real-time implementation of the control algorithm is implemented on dSPACE DS1104. All circuit and control parameters, and operational condition changes correspond to those in the simulation studies section.

Fig. 18 presents the output current of BDC under the EC and PI controllers. As demonstrated in the experimental measurements, the BDC system operating under the EC strategy exhibits no overshoot during mode transitions. In contrast, the PI control exhibits a current overshoot of 0.15 A under identical operational conditions. Furthermore, the BDC regulated by EC demonstrates superior dynamic response performance compared to its PI controlled counterpart, achieving faster dynamic convergence during operational mode switching. Fig. 19 demonstrates that the proposed EC-DDC effectively maintains system stability under both grid frequency fluctuations and harmonic background interference. Fig. 19(a) and (b) validate the robustness of the method under frequency disturbances and grid harmonic conditions, respectively, consistent with the simulation findings presented in Section IV.B. Similarly, Fig. 20 presents the comparison of power when using the PI, MPC and EC-DDC and the output current under EC-DDC. The results demonstrate satisfactory control performance of the designed controller, thereby validating the effectiveness of EC-DDC. When handling three representative operational scenarios, the EC-DDC regulated system exhibits superior dynamic response characteristics with accelerated convergence, smooth power tracking trajectories, and effectively alleviates current stress on power switching devices. These collective findings substantiate the superiority of the proposed EC-DDC in achieving robust operational adaptability and improved power quality. In summary, as shown in Table II, the EC-DDC method achieves a favorable balance between control performance and computational complexity, offering faster dynamic response and lower THD compared to both PI and

MPC approaches. With comparable computational load to PI control and without requiring a PLL, EC-DDC demonstrates superior efficiency and harmonic suppression, validating its effectiveness in practical applications.

VI. Conclusion

This paper has proposed an EC strategy for power converters in PV-battery microgrids. The primary motivation is to address the long-standing challenge of simultaneously achieving fast dynamic response, operation at a fixed switching frequency, and high robustness without relying on PLLs. This combination remains difficult to attain with conventional linear or nonlinear control methods. Additionally, an improved EC-DDC method is proposed to address phase shift and harmonic distortion issues. Based on the simulation and experimental results, the following conclusions are drawn. Firstly, the EC strategy achieves faster tracking performance in both BESS and PV system, outstanding decoupled control performance of active and reactive power without using PLL. It is expected to mitigate the oscillation issues of renewable sources caused by PLL component, thereby offering new insights and technical support for the stable operation of PV-battery microgrids. Secondly, the absence of output overshoot significantly reduces switching losses under high-frequency operation. This mitigates thermal stress on power devices, enhancing system stability while extending device lifespan. Thirdly, the EC-DDC can effectively improve the output power quality of GCI, particularly advantageous due to its simple implementation and ease of operation in terms of harmonic elimination. Finally, by relying solely on software algorithms for harmonic compensation, the proposed method eliminates extra hardware, significantly lowering system cost, size, and complexity.

References

[1] X. Fu, J. Bai, H. Sun, and Y. Zhang, "Optimizing agro-energy-environment synergy in agricultural microgrids through carbon accounting," *IEEE Transactions on Smart Grid*, vol. 15, no. 5, pp. 4819–4834, 2024.

[2] X. Xu, K. Xiahou, W. Du, Y. Liu, Z. Li, Z. Liu, and Q. H. Wu, "Security assessment of cascading failures in cyber-physical power systems with wind power penetration," *IEEE Transactions on Power Systems*, pp. 1–13, 2025.

[3] L. W. Chong, Y. W. Wong, R. K. Rajkumar, R. K. Rajkumar, and D. Isa, "Hybrid energy storage systems and control strategies for stand-alone renewable energy power systems," *Renewable and Sustainable Energy Reviews*, vol. 66, no. DEC., pp. 174–189, 2016.

[4] D. I. Brandao, M. G. Simões, F. A. Farret, H. M. A. Antunes, and S. M. Silva, "Distributed generation systems: an approach in instrumentation and monitoring," *Electric Power Components and Systems*, vol. 46, no. 19-20, pp. 2189–2202, 2018.

[5] A. J. A. Peas Lopec, B. N. Hatziargyiou, C. J. Mutale, C. P. Djapic, and C. N. Jenkins, "Integrating distributed generation into electric power systems: A review of drivers, challenges and opportunities," *Electric Power Systems Research*, vol. 77, no. 9, pp. 1189–1203, 2007.

[6] H. Mahmood, D. Michaelson, and J. Jiang, "Decentralized power management of a pv/battery hybrid unit in a droop-controlled islanded microgrid," *IEEE Transactions on Power Electronics*, vol. 30, no. 12, pp. 7215–7229, 2015.

[7] S. Bhattacharyya and B. Singh, "Battery-supported gfc based microgrid with integration of dfig and pv generation," *IEEE Transactions on Industrial Informatics*, vol. 21, no. 2, pp. 1911–1920, 2025.

[8] W. Gao, K. Xiahou, Y. Liu, Z. Li, Q. H. Wu, D. Chang, and Y. Zhu, "Transient frequency-voltage support strategy for vsc-mtdc integrated offshore wind farms based on perturbation observer and funnel control," *IEEE Transactions on Sustainable Energy*, pp. 1–13, 2025.

[9] K. Xiahou, W. Du, X. Xu, Z. Lin, Y. Liu, Z. Liu, and Q. H. Wu, "Resilience assessment for hybrid ac/dc cyber-physical power systems under cascading failures," *IEEE Transactions on Reliability*, pp. 1–12, 2025.

[10] P. Sumathi and P. A. Janakiraman, "Integrated phase-locking scheme for sdft-based harmonic analysis of periodic signals," *IEEE Transactions on Circuits and Systems II: Express Briefs*, vol. 55, no. 1, pp. 51–55, 2008.

[11] M. S. Reza, M. Ciobotaru, and V. G. Agelidis, "Accurate estimation of single-phase grid voltage parameters under distorted conditions," *IEEE Transactions on Power Delivery*, vol. 29, no. 3, pp. 1138–1146, 2014.

[12] Z. Wang, H. Yi, F. Zhuo, J. Wu, and C. Zhu, "Analysis of parameter influence on transient active power circulation among different generation units in microgrid," *IEEE Transactions on Industrial Electronics*, vol. 68, no. 1, pp. 248–257, 2021.

[13] L. Tao, J. Sun, Z. Tian, M. Huang, X. Zha, and J. Gong, "Speed-sensorless and motor parameters-free starting method for large-capacity synchronous machines based on virtual synchronous generator technology," *IEEE Transactions on Industrial Electronics*, vol. 68, no. 8, pp. 6607–6618, 2021.

[14] X. Xiong, C. Wu, and F. Blaabjerg, "Effects of virtual resistance on transient stability of virtual synchronous generators under grid voltage sag," *IEEE Transactions on Industrial Electronics*, vol. 69, no. 5, pp. 4754–4764, 2022.

[15] J. Dannehl, C. Wessels, and F. W. Fuchs, "Limitations of voltage-oriented pi current control of grid-connected pwm rectifiers with lcl filters," *IEEE Transactions on Industrial Electronics*, vol. 56, no. 2, pp. 380–388, 2009.

[16] Y. Xia, Y. Xu, and X. Feng, "Hierarchical coordination of networked-microgrids toward decentralized operation: A safe deep reinforcement learning method," *IEEE Transactions on Sustainable Energy*, vol. 15, no. 3, pp. 1981–1993, 2024.

[17] M. Hajihosseini, M. Andalibi, M. Gheisarnejad, H. Farsizadeh, and M. H. Khooban, "Dc/dc power converter control-based deep machine learning techniques: Real-time implementation," *IEEE Transactions on Power Electronics*, vol. 35, no. 10, pp. 9971–9977, 2020.

[18] Y. Zeng, J. Pou, C. Sun, X. Li, G. Liang, Y. Xia, S. Mukherjee, and A. K. Gupta, "Deep reinforcement learning-enabled distributed uniform control for a dc solid state transformer in dc microgrid," *IEEE Transactions on Industrial Electronics*, vol. 71, no. 6, pp. 5818–5829, 2024.

[19] O. B. Anderson, B. C. Barry, D. N. Hogan, and M. C. Duffy, "Hysteretic current mode control of a wide output voltage three-level converter," *IEEE Transactions on Power Electronics*, vol. 40, no. 5, pp. 6771–6786, 2025.

[20] R. Viswadev, A. Mudlapur, V. V. Ramana, B. Venkatesaperumal, and S. Mishra, "A novel ac current sensorless hysteresis control for grid-tie inverters," *IEEE Transactions on Circuits and Systems II: Express Briefs*, vol. 67, no. 11, pp. 2577–2581, 2020.

[21] Y. Li, A. J. Watson, and M. Kaya, "A class-e-based multichannel auxiliary power supply with individual hysteresis control," *IEEE Journal of Emerging and Selected Topics in Power Electronics*, vol. 11, no. 3, pp. 3335–3347, 2023.

[22] J. Hu, Q. Sun, R. Wang, B. Wang, M. Zhai, and H. Zhang, "Privacy-preserving sliding mode control for voltage restoration of ac microgrids based on output mask approach," *IEEE Transactions on Industrial Informatics*, vol. 18, no. 10, pp. 6818–6827, 2022.

[23] M. B. Delghavi and A. Yazdani, "Sliding-mode control of ac voltages and currents of dispatchable distributed energy resources in master-slave-organized inverter-based microgrids," *IEEE Transactions on Smart Grid*, vol. 10, no. 1, pp. 980–991, 2019.

[24] X. Chen, Y. Liu, Q. H. Wu, C. Hong, and Y. Su, "Direct power regulation of grid-connected voltage-source inverters based on bang-bang funnel control," *IEEE Transactions on Industrial Electronics*, vol. 71, no. 7, pp. 6460–6470, 2024.

[25] B. Long, Y. Liao, K. T. Chong, J. RodrÃguez, and J. M. Guerrero, "Enhancement of frequency regulation in ac microgrid: A fuzzy-mpc controlled virtual synchronous generator," *IEEE Transactions on Smart Grid*, vol. 12, no. 4, pp. 3138–3149, 2021.

[26] R. Samsami, H. Mirshekali, R. Dashti, M. M. Arefi, and H. R. Shaker, "Robust model predictive control of uncertain dc microgrids based on improved adaptive consensus algorithm," *IEEE Transactions on Industrial Informatics*, vol. 20, no. 11, pp. 13 486–13 497, 2024.

[27] D. Kong, X. Gao, Z. Zhang, C. Liu, M. L. Heldwein, and R. Kennel, "Minimization of current stress for dual active bridge converters based on model predictive control with enhanced zvs ability," *IEEE Transactions on Industrial Electronics*, vol. 71, no. 8, pp. 8970–8980, 2024.

[28] T. Geyer, *Model predictive control of high power converters and industrial drives*. John Wiley & Sons, 2016.
[29] C. Fan, K. Xiahou, L. Wang, and Q. H. Wu, "Data-driven fault detection of multiple open-circuit faults for mmc systems based on long short-term memory networks," *CSEE Journal of Power and Energy Systems*, vol. 10, no. 4, pp. 1563–1574, 2024.
[30] X. Liu, L. Qiu, Y. Fang, and J. RodrÃguez, "Predictor-based data-driven model-free adaptive predictive control of power converters using machine learning," *IEEE Transactions on Industrial Electronics*, vol. 70, no. 8, pp. 7591–7603, 2022.
[31] N. Mohan, T. M. Undeland, and W. P. Robbins, "Power electronics, converters, applications and design," *Microelectronics Journal*, vol. 28, no. 1, 1995.

Zhijun Zeng received the B.E. degree in electrical engineering from the Queen's University of Belfast (QUB), Belfast, U.K., in 2020, and the M.Sc. degree in power system, University College London, London, U.K., in 2021.

He is currently working toward the Ph.D. degree in electrical engineering with the South China University of Technology, Guangzhou, China.

Kaishun Xiahou received the B.E. degree in automation from Guangxi University, Nanning, China, in 2012, and the Ph.D. degree in electrical engineering, from the South China University of Technology, Guangzhou, China, in 2018.

He is currently an Associate Professor with the South China University of Technology. His research interests include anomaly detection, resilient control, nonlinear control in cyber-physical power systems and renewable energy generation systems.

Yang Liu received the B.E. and Ph.D. degrees in electrical engineering from the South China University of Technology, Guangzhou, China, in 2012 and 2017, respectively. He is currently an Associate Professor with the School of Electric Power Engineering, SCUT. He has authored or coauthored more than 30 peer-reviewed SCI journal papers.

His research interests include power system stability analysis and control, nonlinear control theory.

Lei Wang received the B.Eng. and M.Sc. degrees in electrical engineering from Chongqing University, Chongqing, China, in 2008 and 2011, respectively, and the Ph.D. degree in electrical engineering from the South China University of Technology, Guangzhou, China, in 2016.

She is currently a Lecturer with Guangzhou Maritime University, Guangzhou. Her research interests include modeling and control of power converters, and nonlinear analysis of power electronics.

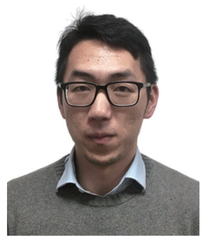

Chuanyue Li received dual B.Eng. degrees from Cardiff University, UK, and North China Electric Power University, China, in 2013, followed by a Ph.D. from Cardiff University in 2017. In 2018, he worked as a postdoctoral researcher at the Laboratory of Electrical Engineering and Power Electronics in Lille, France.

He is currently a Research Associate at the School of Engineering, Cardiff University, Wales, UK. His research interests include the stability and control of power electronics.

Jun Liang received the B.Sc. degree from Huazhong University of Science and Technology, Wuhan China in 1992, and the M.Sc. and Ph.D. degrees from China Electric Power Research Institute, Beijing China in 1995 and 1998, respectively.

Currently, he is a Professor at the School of Engineering, Cardiff University, Wales UK. His research interests include DC technologies, power electronics, power system stability control, and renewable power generation.

Q. H. Wu received the Ph.D. degree in electrical engineering from the Queen's University of Belfast, Belfast, U.K., in 1987.

From 1987 to 1991, he was a Research Fellow and a Senior Research Fellow with QUB. In 1991, he was a Lecturer and Senior Lecturer with the Department of Mathematical Sciences, Loughborough University, Loughborough, U.K. In 1995, he joined the University of Liverpool, Liverpool, U.K., to take up his appointment to the Chair of Electrical Engineering with the Department of Electrical Engineering and Electronics. He is a Chartered Engineer with the Institute of Measurement Control (InstMC), London, U.K. He is currently a Distinguished Professor with the School of Electric Power Engineering, South China University of Technology, Guangzhou, China, where he is also the Director of the Energy Research Institute.

He is currently a Distinguished Professor and Director of the Energy Research Institute at South China University of Technology, China. His research interests include nonlinear adaptive control, mathematical morphology, and evolutionary computation.